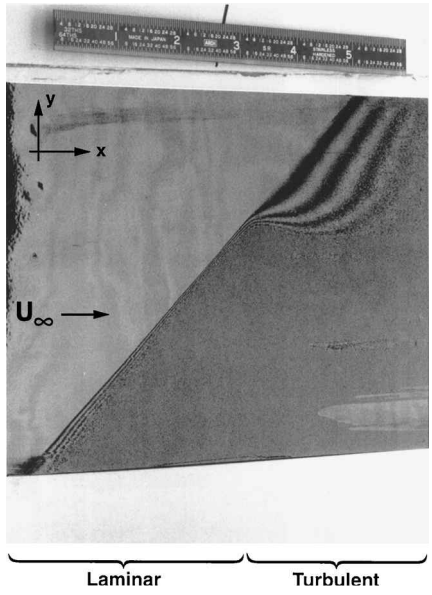

Fig. 4 Interference image showing boundary-layer transition from flight 2.

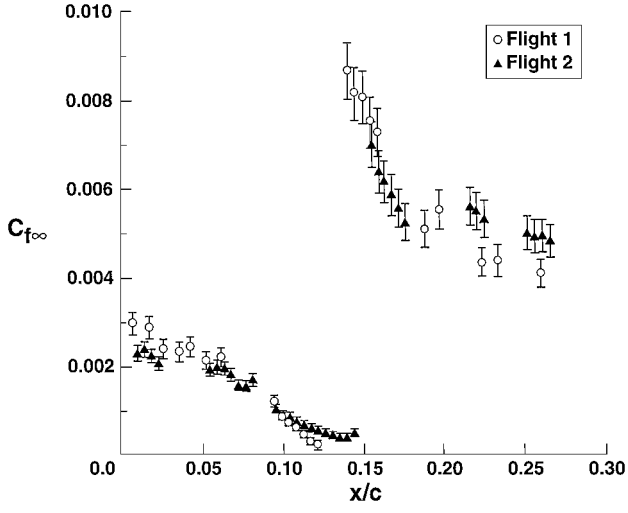

Fig. 5 Chordwise distribution of skin friction coefficient ($C_{f\infty}$ is the local shear stress normalized by the freestream dynamic pressure) at midsemispan for flights 1 and 2.

Conclusions

Oil film interferometry proved easier to use in a flight-test environment than anticipated, and interference fringe images sufficient to allow determination of skin friction within ±10% uncertainty were obtained for each flight at nearly all oil line locations. The location of boundary-layer transition was evident from abrupt change in fringe spacing.

Despite the relatively simple nature of the instrumentation and data recording used in this experiment, it was possible to obtain skin friction measurements at a large number of locations simultaneously. Using self-adhesive Mylar sheets to provide an optical surface made it possible to measure skin friction without modification of the aircraft. This method offers the possibility of making detailed skin friction measurements in flight testing more cheaply and easily than is possible with other methods.

Acknowledgments

This work was supported by Raytheon Aircraft Co. and by the High-Speed Aerodynamics Branch at NASA Ames Research Center.

References

[1]Tanner, L. H., and Blows, L. G., "A Study of the Motion of Oil Films on Surfaces in Air Flow, with Application to the Measurement of Skin Friction," *Journal of Physics E: Scientific Instruments*, Vol. 9, No. 3, 1976, pp. 194–202.

[2]Tanner, L. H., "A Skin Friction Meter, Using the Viscosity Balance Principle, Suitable for Use with Flat or Curved Metal Surfaces," *Journal of Physics E: Scientific Instruments*, Vol. 10, No. 3, 1977, pp. 278–284.

[3]Tanner, L. H., "A Comparison of the Viscosity Balance and Preston Tube Methods of Skin Friction Measurement," *Journal of Physics E: Scientific Instruments*, Vol. 10, No. 6, 1977, pp. 627–632.

[4]Tanner, L. H., "The Application of Fizeau Interferometry of Oil Films to the Study of Surface Flow Phenomena," *Optics and Lasers in Engineering*, Vol. 2, No. 1, 1981, pp. 105–118.

[5]Monson, D. J., Mateer, G. G., and Menter, F. R., "Boundary-Layer Transition and Global Skin Friction Measurement with an Oil-Fringe Imaging Technique," *SAE Aerotech'93*, Paper 932550, Society of Automotive Engineers, Costa Mesa, CA, Sept. 1993.

[6]Mateer, G. G., Monson, D. J., and Menter, F., "Shear and Pressure Measurements on an Airfoil at Angle of Attack," AIAA Paper 95-2192, June 1995.

[7]Mateer, G. G., Monson, D. J., and Menter, F., "Skin-Friction Measurements and Calculations on a Lifting Airfoil," *AIAA Journal*, Vol. 34, No. 2, 1996, pp. 231–236.

[8]Kennelly, R. A., Jr., Westphal, R. V., Mateer, G. G., and Seelen, J., "Surface Oil Film Interferometry on a Swept Wing Model in Supersonic Flow," *Proceedings of the Seventh International Symposium on Flow Visualization*, edited by J. P. Crowder, Begell House, New York, 1995, pp. 302–307.

Dynamic Unstructured Method for Relative Motion of Multibody Configuration at Hypersonic Speeds

Oktay Baysal* and Xiaobing Luo†
Old Dominion University, Norfolk, Virginia 23529-0247

Introduction

A WIDE variety of engineering problems include time-dependent flowfields resulting from the relative motion of multibody configurations. The fluid forces and the moments exerted on the involved boundaries, therefore, are unsteady, and they require time-accurate computations on dynamic meshes. Among the examples for such problems are rotor–stator interaction, rotorcraft dynamics, store separation, detachment of multistage-rocket components, separation of booster tanks from the space shuttle, piston motion in internal combustion engines, and heart valve and blood flow interaction.

Only recently, we have seen the emergence of methodologies to solve such problems. Examples by the prominent researchers of this topic may be found in Ref. 1. All of these solutions often require impractical amounts of computing time and resources. A discussion of the two competing approaches developed by the present authors can be found in Ref. 2. The present dynamic unstructured technique (DUT) method was initially developed[3,4] as an explicit time-integration method for flow speeds up to Mach 1.5. The present Note will report on the significant improvements that removed this restriction and increased its computational efficiency by an order of magnitude.

Presented as Paper 98-2412 at the AIAA 16th Applied Aerodynamics Conference, Albuquerque, NM, 15–18 June 1998; received 27 August 1998; accepted for publication 15 March 1999.

*Professor and Eminent Scholar, Aerospace Engineering Department; obaysal@odu.edu. Associate Fellow AIAA.

†Graduate Research Assistant, Aerospace Engineering Department.

After some comparisons with experimental data, the improved DUT has been applied in simulating the separation of a hypersonic research vehicle from its booster rocket. Because the currently ongoing Hyper-X program motivated this example, a very brief background will be presented next. The goal is to demonstrate the technology, experimental and computational methods, and tools for design and performance predictions of a hypersonic vehicle with an airframe integrated scramjet propulsion system.[5] The Hyper-X research vehicle is 12 ft long and has a 5-ft wingspan with scheduled flights at Mach 5, 7, and 10. A rocket will be used as the launch vehicle, which will boost the research vehicle to an altitude with a dynamic pressure of 1000 lb/ft^2. The research vehicle will be mounted on an arm attached to the nose of the launch vehicle. The stage separation will resume with the ignition of the explodable rivets fastening the vehicle to the arm. Then, the arm will swing down about its hinge leaving the research vehicle free and airborne at the desired flight speed. During this arm motion, a complex shock structure is expected, which, subsequently, should cause an unsteady aerodynamic interference.

The second objective of the present paper is to demonstrate the suitability of DUT in predicting this unsteady hypersonic flowfield, which, in turn, should lead to a closer scrutiny of the resulting dynamic loads on the vehicle.

Methodology

In the baseline DUT[3,4] the upwind-discretized form of the governing equations was integrated in time using an explicit four-stage Runge–Kutta method. To avoid grid-motion-induced error, the geometric conservation law was satisfied concurrently with the conservation equations. For the adaptation of the mesh to the boundary motion, the tension-springs analogy[6,7] was used. To restrict the size of the adaptation region, a window was created around a moving body. Only the window points were adapted, but the nodes exterior to the window were spatially fixed in time. Recently, major improvements have been incorporated,[8,9] and these will be briefly discussed next.

First, to enhance the quality of the conforming mesh as a body moved, the mesh smoothing using the Jacobi method followed the mesh adaptation within a window. Then, the mesh was optimized for a target area distribution.[8,10] This has by and large alleviated otherwise conceivable mesh tangling problems during the relatively large increments of body motion per mesh update. Hence, the motion could be covered with a less number of mesh updates.

Secondly, a second-order-accurate implicit time integration, which employed dual-time steps for unsteady flows, was extended for relative moving body problems. Consequently, the time-accurate steps were significantly larger than those for the explicit

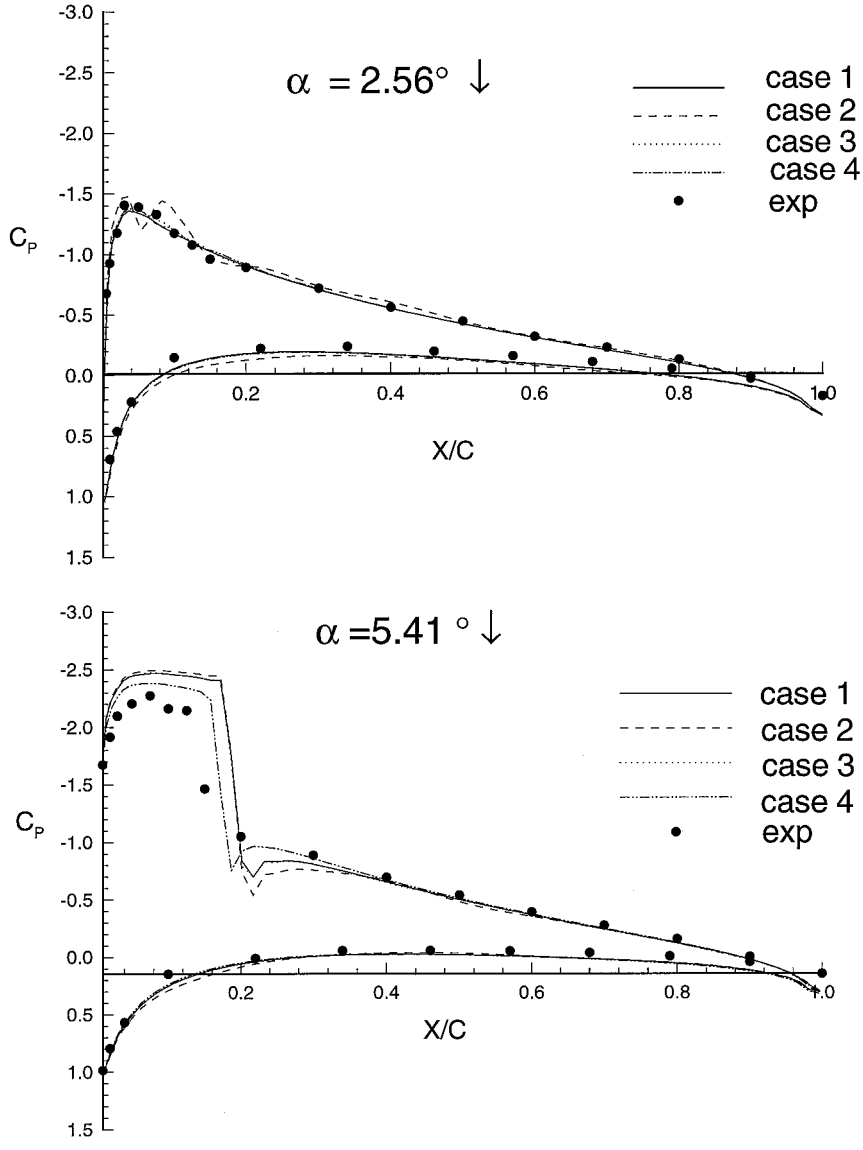

Fig. 1 Pressure coefficient distributions on sinusoidally pitching NACA 0012 airfoil at two pitch-down instants compared with experimental data.[12] Explicit scheme (case 1), implicit scheme on single mesh (case 2), implicit multigrid scheme on two-level meshes (case 3), and implicit multigrid scheme on three-level meshes (case 4).

Runge–Kutta time integration method of the baseline DUT. Denoting the vector of conserved fluid flow variables by Q and a finite volume area by V, the integral form of the two-dimensional, unsteady Euler equations were integrated using a three-point backward-difference formula:

$$L[(VQ)^{n+1}] = S \tag{1}$$

where L and S denote an operator and a source, respectively,

$$L[(VQ)^{n+1}] \equiv (3/2\Delta t)(VQ)^{n+1} + R(Q^{n+1}) \tag{2}$$

and

$$S = (2/\Delta t)(VQ)^{n} - (1/2\Delta t)(VQ)^{n-1} \tag{3}$$

The residual R was constructed as the computed sum of the fluxes F through the cell edges. Considering U as an approximation to Q, an unsteady residual $R^*(U^{n+1})$ was defined from Eq. (1). The resulting nonlinear system was first augmented by a pseudotime term (Δt^* denotes local pseudotime step), then solved by a low-storage, ϑ (2)-accurate, m-stage implicit Runge–Kutta scheme:

$$\left[I + (3/2\Delta t)\alpha_i \Delta t^*\right] V^{n+1} Q^{(i)} = V^{n+1} Q^{(0)} - \alpha_i \Delta t^* \left[R\left(Q^{(i-1)}\right) - S\right] \tag{4}$$

where

$$\alpha_i = \frac{1}{m-i+1}, \qquad i = 1, \ldots, m$$
$$Q^{(0)} \leftarrow U^n, \qquad U^{n+1} \leftarrow Q^{(m)} \tag{5}$$

The baseline DUT had employed either the van Leer flux-vector splitting or the Roe flux-differences splitting to obtain the upwind discretization, and no limiters were used for the higher-order scheme. This method, however, experienced severe numerical instabilities for hypersonic flows with strong shocks. Hence, the flux-vector splitting because of Hänel[11] with van Albada limiter was used to improve the stability:

$$F(Q) = F^+(Q^-) + F^-(Q^+) \tag{6}$$

where

$$F^{\pm}(Q^{\mp}) \cdot \hat{n} = \rho u_n^{\pm} [1 \quad u_x \quad u_y \quad H]^t + p^{\pm} [0 \quad n_x \quad n_y \quad 0]^t \tag{7}$$

$$u_n^{\pm} = \begin{cases} \pm \dfrac{(u_n \pm c)^2}{4c}, & \text{if } |u_n| \le c \\ \dfrac{(u_n \pm |u_n|)}{2}, & \text{else} \end{cases}$$
$$p_n^{\pm} = \begin{cases} (p/4)[(u_n/c) \pm 1]^2 [2 \mp (u_n/c)] \\ p(u_n \pm |u_n|)/2u_n \end{cases} \tag{8}$$

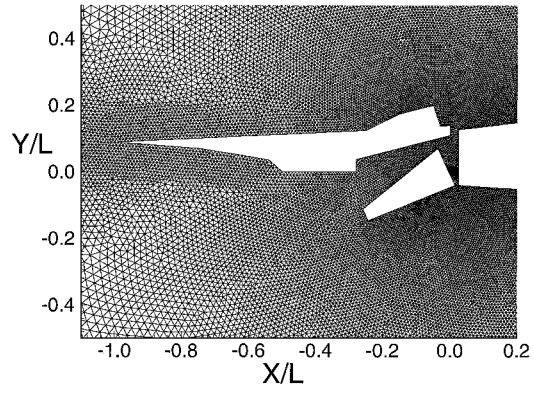

a) Two-dimensional, dynamic, unstructured mesh

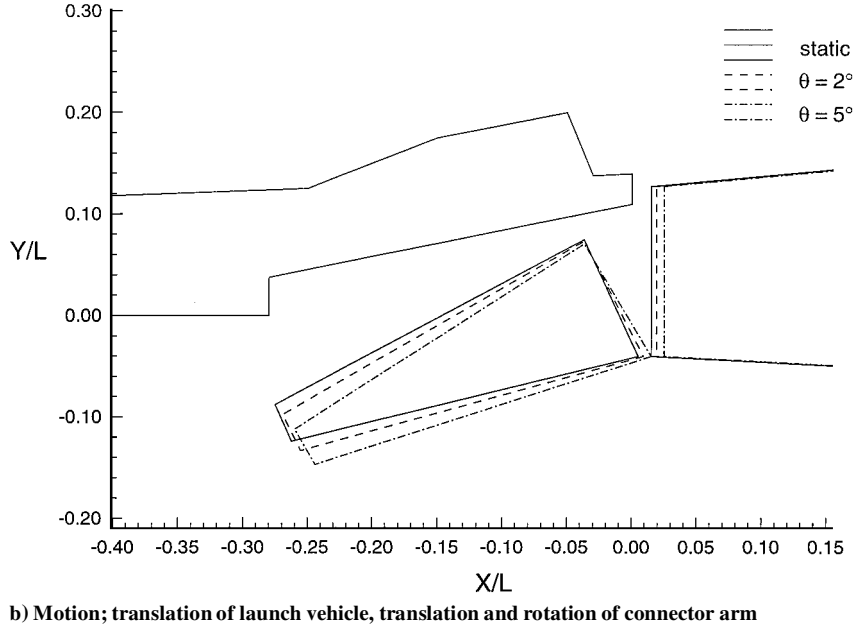

b) Motion; translation of launch vehicle, translation and rotation of connector arm

Fig. 2 Assembly of hypersonic research plane, launch vehicle, and connector arm.

To accelerate the convergence of the subiterations [Eq. (4)], an overset-type multigrid method with full-approximation scheme was developed. The purpose was to transform the slow decaying, low-frequency error component to a higher-frequency error by reconstructing the residual on a coarser mesh. By referring to any pair of sequentially coarsened meshes as fine and coarse meshes, the method may be summarized as follows. When Eq. (4) was solved on a coarser mesh, the source term was modified to include the residual of the fine mesh solution:

$$S_c = L_c\left[I^U_{f\to c}\cdot U_f\right] - I^R_{f\to c}\cdot R^*_f(U_f) \tag{9}$$

where $I_{f\to c}$ is a fine-to-coarse restriction operator. Upon obtaining the coarse mesh solution, the fine-mesh solution was then corrected as

$$U_f \leftarrow U_f + I^U_{c\to f}\cdot\left[U_c - \left(I^U_{f\to c}\cdot U_f\right)\right] \tag{10}$$

where $I_{c\to f}$ is a coarse-to-fine prolongation operator. After locating a coarse mesh node in a fine-mesh cell (or vice versa), finding the value of a transferred quantity at the coarse mesh node required solving the equation of the plane at that node. The geometric weights were found in terms of the coordinates of the coarse mesh node and the vertices of the surrounding fine mesh cell. To interpolate the residual from the fine mesh to a coarse mesh conservatively, the weights for the distribution were the same weights used in the linear interpolation from the coarse mesh to the fine mesh. Because the sum of the weights multiplying the residual at any fine mesh node was unity, this ensured that all fine-mesh residuals contributed to the coarse mesh and that the total residual was conserved.

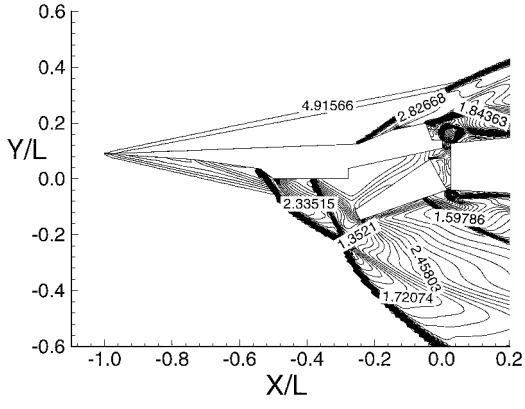

Fig. 3 Instantaneous Mach contours during staging at Mach 5 flight: L = 12 ft, q_∞ = 1000 lbf/ft^2 and θ = 5 deg.

Results

The methodology was first tested through a benchmark case[12]: NACA-0012 airfoil in Mach 0.6 flow was sinusoidally pitched about its quarter chord with a mean incidence of $\alpha_m = 4.86$ deg. The amplitude and the reduced frequency were $\alpha_0 = 2.44$ deg and $k = 0.081$, respectively. The flowfield was first computed using the baseline DUT, that is, an explicit scheme on a single mesh (case 1), then with the present implicit (case 2) scheme. Finally, the computations were repeated on the fine mesh but using the multigrid acceleration with only one coarse mesh (case 3), then with two coarser level meshes (case 4). As shown in Fig. 1, the present method predicted the instantaneous pressure distributions successfully. More importantly, because of the four major improvements just discussed, an order of magnitude computational time saving was realized over the baseline DUT.

Presented in Fig. 2 are the close-up view of the dynamic unstructured mesh and the relative motion of the present demonstration case: hypersonic research plane, its launch vehicle, and the connector arm. The two-dimensional mesh consisted of 69,936 cells, of which only 11,356 were inside the dynamic window. The staging was simulated as a two-degrees-of-freedom motion. The booster and the arm were assigned a translational motion ($\Delta X = V_x t$) and superimposed was the arm's rotation ($\theta = \omega t$). The values for the translational and the rotational velocities were arbitrarily assigned as $V_x = 9.8$ ft/s and $\omega = 7.1$ rad/s, respectively.

The unsteady solution for the Mach 5 flight at $t = 12.2$ ms is depicted in Fig. 3 via its Mach contours. At this instant the distance was $\Delta X = 0.12$ ft and $\theta = 5$ deg. A very complex network of strong shocks, expansions, and their interactions dominated the predicted flowfield. A subsonic, high-pressure region was formed at the inboard between the hypersonic research vehicle and the arm. This resulted in two jets, one bleeding into the base region of the vehicle and the other to the lower surface of the booster nose.

To demonstrate the unsteady aerodynamic interference effects, the pressure coefficient on the research vehicle surface was plotted at various instants (Fig. 4). The time variation was primarily confined to only 5% length on the upper surface, but it stretched out to 20% on the lower surface. As the arm rotated, the pressure rise on the upper surface was larger than that on the lower surface. This resulted in a decreasing normal force, decreasing pitching moment (about its area centroid), but the thrust (negative of axial force) kept increasing (Fig. 5).

Although this separation was also computed for a Mach 10 flight,[9] it is not included herein for brevity. Also, neither the three-dimensional computer code was developed nor the exact geometry

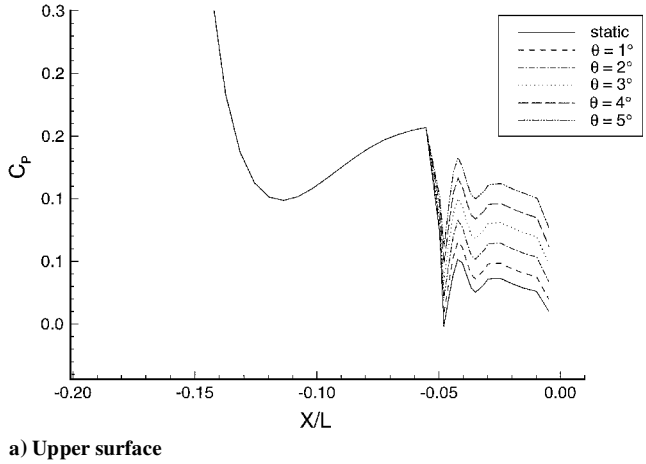

a) Upper surface

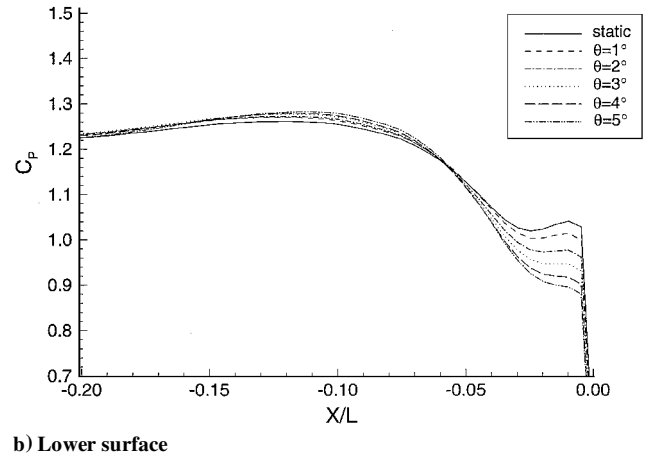

b) Lower surface

Fig. 4 Pressure coefficient distributions at various instants over the aft 20% of airplane length depicting unsteady interference effects.

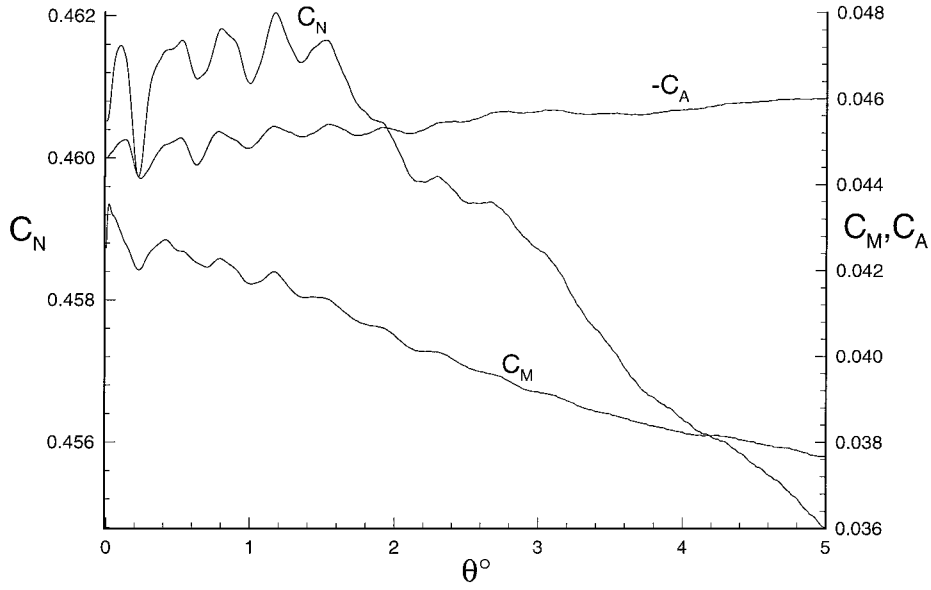

Fig. 5 Histories of force and moment coefficients on hypersonic plane during staging at Mach 5 flight. Pitching center at area centroid: $X_C = -0.466$ and $Y_C = 0.089$.

was available. Hence, the present proof-of-concept simulation was based on the two-dimensional Euler equations solved for an approximate geometry. A more realistic modeling would require the three-dimensional computations including the diffusion terms for the exact geometry. This is currently being pursued.

References

[1]Sakell, L., and Knight, D. D. (eds.), *Proceedings of the First AFOSR Conference on Dynamic Motion Computational Fluid Dynamics*, Rutgers Univ., New Brunswick, NJ, 1996.

[2]Baysal, O., Singh, K. P., and Yen, G.-W., "Dynamic CFD Methods for Prescribed and Aerodynamically-Determined Relative-Moving Multibody Problems," *Proceedings of the First AFOSR Conference on Dynamic Motion CFD*, edited by L. Sakell and D. Knight, Rutgers Univ., New Brunswick, NJ, 1996, pp. 31–44.

[3]Singh, K. P., and Baysal, O., "3D Unstructured Method for Flows Past Bodies in 6-DOF Relative Motion," *Proceedings of 6th International Symposium on CFD*, edited by M. Hafez, Vol. 3, Univ. of California, Davis, CA, 1995, pp. 1161–1168.

[4]Singh, K. P., Newman, J. C., III, and Baysal, O., "Dynamic Unstructured Method for Flows Past Multiple Objects in Relative Motion," *AIAA Journal*, Vol. 33, No. 4, 1995, pp. 641–659.

[5]Rausch, V. L., McClinton, C. R., and Hicks, J. W., "Scramjets Breathe New Life into Hypersonics," *Aerospace America*, Vol. 35, No. 7, 1997, pp. 40–46.

[6]Batina, J. T., "Unsteady Euler Airfoil Solutions Using Unstructured Dynamic Meshes," AIAA Paper 89-0115, Jan. 1989.

[7]Baysal, O., "Flow Analysis and Design Optimization Methods for Nozzle-Afterbody of a Hypersonic Vehicle," *Computational Methods in Hypersonic Aerodynamics*, Kluwer, Dordrecht, The Netherlands, 1992, pp. 341–386.

[8]Baysal, O., and Luo, X.-B., "Computational Aeromechanics Method with Multigrid Accelerated Dual Time Stepping on Unstructured Meshes," *Proceedings of American Society of Mechanical Engineers Fluids Engineering Division Summer Meeting*, American Society of Mechanical Engineers, New York, FEDSM-98-4939, 1998.

[9]Baysal, O., and Luo, X.-B., "Staging of a Hypersonic Vehicle: Numerical Simulations Using Dynamic Unstructured Meshes," *Proceedings of 16th AIAA Applied Aerodynamics Conference*, Reston, VA, 1998, pp. 85–95.

[10]Pirzadeh, S., "Recent Progress in Unstructured Grid Generation," AIAA Paper 92-0445, Jan. 1992.

[11]Hänel, D., Schwane, R., and Seider, G., "On the Accuracy of Upwind Schemes for the Solution of the Navier–Stokes Equations," AIAA Paper 87-1005, Jan. 1987.

[12]Landon, R., "NACA 0012 Oscillatory and Transient Pitching," *Compendium of Unsteady Aerodynamic Measurements*, AGARD Rept. 702, 1982, pp. 3.3–3.25.

V-Tail Stalling at Combined Angles of Attack and Sideslip

Malcolm J. Abzug*
Pacific Palisades, California 90272

Introduction

POSSIBLE stalling of V-tail panels at large combined angles of attack and sideslip has been a concern in flight operations. V-tail panel angles of attack developed by Purser and Campbell[1] apply only to small angles of attack and sideslip. Small-angle results are useful for tail sizing and the calculation of stability derivatives, but this Note extends the Purser and Campbell work to large angles to support studies of possible panel stalling.

Panel Angle-of-Attack Derivation

The geometric angle of attack of a V-tail panel is the angle the local wind makes with a tail chord line, measured in the plane of the airfoil. Neglecting angular velocity, the geometric angles of attack and sideslip of a single V-tail panel are a function only of the following six variables: α and β, the aircraft angles of attack and sideslip; ε and σ, the average downwash and sidewash angles at the V-tail; Γ, the dihedral angle of a V-tail panel, positive for the left panel; and δ, the V-tail incidence or control angle for an all-moving V-tail.

The panel geometric angles of attack and sideslip are found by the matrix operations[2] of Eqs. (1–3). Panel body axes are fixed in the panel with X forward in the chord plane, Z normal to the chord plane pointing down, and Y pointing to the right. Equation (1) represents successive rotations of panel body axes away from aircraft wind axes. In the wind axes used here the X axis points into the relative wind, and X–Z is an aircraft plane of symmetry.

The first two rotations carry aircraft body axes away from wind axes by $\beta + \sigma$ and then $\alpha - \varepsilon$. The third and fourth rotations Γ and then δ establish panel body axes. Tail panel angles of attack and sideslip are found from the wind vector components in the final, rotated position of panel axes. The incidence or control angle δ

Received 27 July 1998; revision received 20 March 1999; accepted for publication 20 March 1999.

*Aeronautical Consultant, 14951 Camarosa Drive. Fellow AIAA.